

Accelerating Binarized Neural Networks via Bit-Tensor-Cores in Turing GPUs

Ang Li and Simon Su

Abstract—Despite foreseeing tremendous speedups over conventional deep neural networks, the performance advantage of binarized neural networks (BNNs) has merely been showcased on general-purpose processors such as CPUs and GPUs. In fact, due to being unable to leverage bit-level-parallelism with a word-based architecture, GPUs have been criticized for extremely low utilization (1%) when executing BNNs. Consequently, the latest tensorcores in NVIDIA Turing GPUs start to experimentally support bit computation. In this work, we look into this brand new bit computation capability and characterize its unique features. We show that the stride of memory access can significantly affect performance delivery and a data-format co-design is highly desired to support the tensorcores for achieving superior performance than existing software solutions without tensorcores. We realize the tensorcore-accelerated BNN design, particularly the major functions for fully-connect and convolution layers — bit matrix multiplication and bit convolution. Evaluations on two NVIDIA Turing GPUs show that, with ResNet-18, our BTC-BNN design can process ImageNet at a rate of 5.6K images per second, 77% faster than state-of-the-art. Our BNN approach is released on <https://github.com/pnnl/TCBNN>.



1 INTRODUCTION

BINARIZED-neural-network (BNN) [1], [2], [3] is an alternative type of deep-neural-networks (DNNs). Compared to general DNNs, such as multi-layer-perceptrons (MLPs) and convolution-neural-networks (CNNs), the major difference of BNN is that it uses a single bit to represent each entry of the input and weight matrices. BNN evolved from DNN through binarized-weight-network (BWN) [4]. It was firstly observed that if the weight matrix can be binarized to $+1$ and -1 , the floating-point (FP) multiplications can be degraded to addition (i.e., `mul +1`) and subtraction (i.e., `mul -1`). Later, it was further observed that if the input matrix can be binarized as well, then even the floating-point additions and subtractions in BWN can be degraded to logical operations (i.e., `xnor` for bit dot-product and `popc` for bit accumulation) [1], [2], [3].

BNNs bring several advantages over full-precision DNNs: (a) *Reduced and simplified computation*. Through binarization, each segment of 32 FP fused-multiply-add (FMA) operations can be aggregated into an `xnor` operation and a `popc` operation, leading to theoretically $16\times$ speedups; (b) *Reduced data movement and storage*. Through binarization, the whole memory hierarchy and network, including registers, caches, scratchpad, DRAM, NoC, etc. can accommodate $32\times$ in both bandwidth and capacity; (c) *Reduced cost* which comprises energy reduction from simplified hardware design and smaller chip area; (d) *Resilience*. It has been reported that compared with differentiable DNNs, the discrete BNNs exhibit superior stability and robustness against adversarial attacks [5], [6].

On the flip side of the coin, binarization reduces the model’s capacity and discretizes the parameter space, lead-

ing to certain accuracy loss. With the tremendous effort from the machine learning community [2], [7], [8], [9], accuracy of BNNs have been dramatically enhanced. The top-1 training accuracy of BNN-based AlexNet and ResNet-18 on ImageNet dataset has achieved 46.1% [8] and 56.4% [10] (54.3% and 61% with boosting [11]), with respect to 56.6% and 69.3% for full-precision DNN [12]. A latest BNN work even reported a top-1 accuracy of 70.7% [13].

Although BNN is not likely to substitute DNNs because of reduced model capacity, for many HPC [14], [15], [16], [17] and cloud applications [18], [19], when certain accuracy levels can be achieved, alternative factors such as latency, energy, hardware cost, resilience, etc. become more prominent. This is especially the case for practical deployment.

Despite featuring various advantages, the expected performance gain of BNN has rarely been demonstrated on general purpose processors such as GPUs. This is mainly because: (i) the fundamental design mismatch between bit-based algorithms and word-based architecture; (ii) BNN designs at this stage are mainly driven by the algorithm community on how to improve training accuracy; little system and architectural support have been provided on high performance delivery. Due to (i), most existing BNN implementations are realized as hardware accelerators (e.g., through FPGA [20], [21], [22], [23], [24], [25]) where the operand bit-width can be flexibly adjusted. Due to (ii), BNN developers are still relying on full-precision software frameworks such as TensorFlow and PyTorch over CPUs and GPUs to emulate the BNN execution. As a result, the lack of architectural & system support hinders the performance delivery and the general adoption of BNNs.

This situation has been lately changed for GPUs. On the software side, a recent work [26] proposed the so-called binarized software tensor core or BSTC, relying on GPU’s low-level hardware intrinsics for efficient 2D bit-block processing, such as *bit matrix multiplication* (BMM) and *bit convolution* (BConv). On the hardware side, the latest NVIDIA Turing GPUs started to support BMM experimen-

- A. Li is a computer scientist from the High-performance Computing group of Pacific Northwest National Laboratory (PNNL), Richland, WA, 99354. E-mail: ang.li@pnnl.gov, see <http://www.angli.phd.com>
- S. Su is a computer scientist from the DoD Supercomputing Resource Center of U.S. Army Research Laboratory (ARL), Aberdeen Proving Ground, MD, 21005.

TABLE 1: Bit-Software-Tensor-Core (BSTC) [26] vs. Bit-Tensorcore (BTC). *uint32* refers to *unsigned int*. *uint64* refers to *unsigned long long int*. *INTU* refer to *integer units*. *SFU* refers to *special function units*.

| Datatype | BSTC Bit (uint32, uint64) | BTC Bit (uint32) |
|------------------|------------------------------|---------------------------|
| Functionality | Bit Matrix Multiplication | Bit Matrix Multiplication |
| Tile-A size | 32×32 or 64×64 | 8×128 |
| Tile-B size | 32×32 or 64×64 | 128×8 |
| Tile-C size | 32×32 or 64×64 | 8×8 |
| Hardware units | INTUs and SFUs | TensorCore Units (TCUs) |
| Processing level | per warp | per warp |
| GPU Platforms | Kepler or later (≥CC-3.0) | Turing GPUs (≥CC-7.5) |

tally in their *Tensor Core Units* (TCUs) [27]. We label this new bit-capability as Bit-Tensor-Core, or BTC. Table 1 compares the major features of BSTC and BTC.

In this work, we focus on these bit-tensorcores in Turing GPUs and investigate how they can be fully leveraged for advanced performance delivery for BNNs. This paper thus makes the following major **contributions**: (i) To the best of our knowledge, this is the first work to investigate this brand new bit-computation capability of GPU tensorcores¹. We designed orchestrated microbenchmarks to investigate the low-level features of BTC. In particular, we observed that the value of stride exhibits considerable performance impact on memory fetch from the global memory via Warp-Matrix-Multiplication-API (WMMMA). (ii) Based on our observations, we proposed a new bit data format specially for bit-computation on GPU tensorcores. We showed that without this new bit format, BTC might not exhibit performance advantage over existing software solutions; (iii) BTC currently only supports XOR-based bit-matrix-multiplication. In terms of convolution, traditional approaches [28], [29] that transform convolution to matrix-multiplication fail to work properly for BNNs due to the challenge in padding [30]. In this work, we propose a new approach that can fully leverage the bit-computation capability of BTC while effectively resolving this padding issue. We evaluated our design on two NVIDIA Turing GPU platforms, the results showed that our BTC-based BMM design could bring up to 4.4× speedup over the vendor’s *Cutlass* [31] implementation. Regarding BNN end-to-end inference performance, compared with state-of-the-art solution [26], our BTC-based approach achieved on average 2.20× and 2.25× in latency, and 1.99× and 1.62× in throughput for VGG-16 and ResNet-18 on ImageNet dataset. Since bit-computation is increasingly common in many HPC and data-analytics scenarios [32], [33], [34], [35], [36], [37], [38], [39], our techniques can be extended to other bit applications.

2 RELATED WORK

We focus on the performance issues of BNN implementation and the GPU tensorcores in this section. Regarding the algorithm design for BNNs, please refer to this survey [30].

BNN Implementation The major purpose of BNN implementation is to leverage the system and architectural features of the platforms to satisfy the stringent latency and throughput constraints when deploying BNNs in HPC, cloud and embedded applications, while reducing the area

¹. To the best of our knowledge, this feature has not appeared in vendor’s library like cuBLAS, cuDNN, TensorRT or other library up to now except *Cutlass* in which it is supported as an experimental, unverified function.

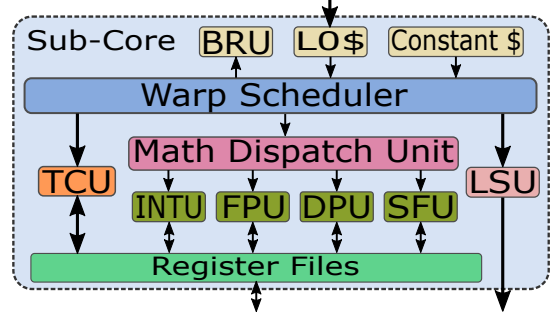


Fig. 1: A subcore of a Turing GPU SM. *BRU* is branch unit. *\$* refers to cache. *LSU* is the load-store-unit. *INTU* is the integer-unit. *FPU* is the floating-point-unit. *DPU* is the double-precision-unit. *SFU* is the special-function-unit. *TCU* is the tensorcore-unit, which has its independent data path.

and energy cost [20], [21], [22], [23], [24], [25], [40], [41]. Most of these implementations focus on FPGA [20], [21], [22], [23], [24], [25] due to FPGA’s design flexibility at the bit level. Regarding general-purpose platforms, an existing CPU work [41] relies on the AVX/SSE vector instructions to derive good bit computation performance. It focuses on BMM and transforms bit-convolution to BMM through *im2col()* with costly pre- and post-processing. Another evaluation work [42] compares CPU, GPU, FPGA and ASIC based BNN designs, clarifying that the major performance restriction of CPUs and GPUs is *the extremely low utilization due to the challenge in extracting fine-grained parallelism*. Noticeably, the reported GPU utilization is 1% only [42]. To improve GPU utilization and extract bit-level-parallelism, a recent work [26] proposed the binarized-soft-tensor-core (BSTC) on top of GPU’s SMs and leverages low-level hardware intrinsics for harvesting the bit-processing capability of GPUs. For BSTC, the performance gains from better utilization of the conventional integer/logic units (i.e., INTUs and SFUs, see Figure 1). This work is different because we focus on the brand new bit computation capability of the latest Turing TCUs, and showcase how to harvest the most performance from this new functional units.

GPU Tensorcore Driven by the demand of training large-scale DNNs, designing specialized low-precision dense matrix-matrix multiplication accelerators has become a popular trend. Particularly, Google presented *Tensor-Processing-Units* (TPUs) [43]; Intel announced the *Nervana Neural-Network-Processors* (NNPs) for tensor operations; NVIDIA integrated the *Tensorcore Units* (TCUs) into their Volta and Turing GPUs; Qualcomm included the *Hexagon-Tensor-Accelerator* (HTA) into their Hexagon 855 system-on-chip.

This work focuses on the tensorcores of GPUs (see Figure 1). Since being firstly introduced in the Volta architecture [44], the tensorcore becomes one of the spot-light for GPGPU research. The relevant works can be summarized in two categories: (a) **Characterization**. In [45] and [46], Jia et al. dissected the Volta (Tesla V100) and the Turing (Tesla T4) GPUs through microbenchmarking. They depicted the detailed mapping mechanism from elements of a matrix tile to registers of a warp-lane in the HMMA instructions for FP16 matrix multiplication. They found that the 32 threads of a warp are essentially divided into 8 thread groups, where the 4 threads per group cooperatively work on the same regions of matrix *C* by fetching elements from different parts of matrix *A* and matrix *B*. Markidis et al. [47] studied the programmability, performance and precision of the

Volta tensorcores and proposed a technique to compensate the accuracy loss due to precision degradation from FP32 to FP16. Raihan et al. [48] investigated the design details of the tensorcores in Volta and Turing GPUs and built an architecture model for the tensorcores in GPGPU-Sim. They characterized the WMMA APIs and clarified how the operand sub-matrix elements were mapped for FP16 GEMM in Volta tensorcores, and FP16/Int8/Int4 GEMM in Turing tensorcores. However, they did not investigate the 1-bit computation mode. Hickmann and Bradford [49] proposed a testing method for assessing the compliance of IEEE standard, hardware microarchitecture, and internal precision of the Volta tensorcores. **(b) Application.** Haidar et al. [50] proposed a mixed-precision iterative refinement method to approach FP64 precision using FP16-based GPU tensorcores in LU factorization, acting as the first effort to apply GPU tensorcores for non-machine-learning applications. Sorna et al. [51] applied FP16 tensorcores for FFT acceleration. Blanchard et al. [52] thoroughly analyzed the rounding error of matrix multiplication and LU factorization when using the tensorcores. Dakkak et al. [53] showed that the tensorcores, which were originally designed for 2D FP16 GEMM, can be adopted for 1D array reduction and scan.

Most of these works, however, focused on FP16 mixed-precision matrix-multiply in Volta tensorcores. They either evaluated their performance, programmability, accuracy, hardware design, or looked into alternative applications other than GEMM, aiming to preserve higher precision. None of them have investigated the latest bit computation capability of the GPU tensorcores. In addition, no existing works have ever reported the potential performance impact from the stride of segmented memory load, and how to circumvent the challenges in accelerating convolutions through the tensorcores. Furthermore, until writing the paper, we have not seen any works leverage GPU tensorcores for the acceleration of BNNs.

3 GPU BIT TENSORCORES

3.1 GPU Tensorcores

Since the Volta architecture (CC-7.0), NVIDIA GPUs have introduced a novel type of function units known as *Tensorcores* into the streaming multiprocessors (SMs) for accelerating low-precision general matrix multiplication (GEMM). In Volta, each tensorcore processes 64 FP16 FMA operations per cycle [54]. The only supported datatype for Volta tensorcores is FP16. For Turing (CC-7.5), more datatypes are supported, including FP16, signed/unsigned int-8, int-4, and recently a bit as well. Please refer to [45], [48], [54] for more details about the hardware features of Volta and Turing GPU tensorcores.

3.2 CUDA WMMA

Since CUDA Runtime-9.0, the *Warp Matrix Multiplication API* (WMMA) has been introduced for operating the tensorcores in Volta and Turing GPUs. The idea is to partition the three input and one output matrices into tiles, where each warp processes the multiplication of one tile ($T_D = T_A \times T_B + T_C$). WMMA provides the necessary primitives to operate on the bit-tiles (e.g., loading input tiles,

```
1 namespace experimental {
2   namespace precision { struct b1; } // define 1-bit datatype
3   enum bmmaBitOp { bmmaBitOpXOR = 1 }; //only XOR is supported as the mul -- op for BTC
4   enum bmmaAccumulateOp { bmmaAccumulateOpPOPC = 1 }; //popc acts as the acc -- op for BTC
```

Listing 1: WMMA 1-bit definition and operations in *crt/mma.h*

```
1 wmma.load.a.sync.aligned.row.m8n8k128.global.b1 { %r21 }, [%rd8], [%r20]; //load_matrix_sync()
2 wmma.load.b.sync.aligned.col.m8n8k128.global.b1 { %r22 }, [%rd5], [%r20]; //load_matrix_sync()
3 wmma.load.c.sync.aligned.row.m8n8k128.global.s32 [%rd30], [%r35,%r64], [%r60]; //load_matrix_sync()
4 wmma.mma.xor.popc.sync.aligned.row.col.m8n8k128.s32.b1.b1.s32 { %r23,%r24 }, { %r21 }, { %r22 },
5   { %r19,%r19 }; //bmma_sync()
6 wmma.store.d.sync.aligned.row.m8n8k128.global.s32 [%rd34], { %r63,%r64 }, [%r60]; //store_matrix_sync()
```

Listing 2: PTX code for Bit-Matrix-Multiply-API (BMMA)

tilled multiplication, storing output tile): *load_matrix_sync*, *mma_sync*, *store_matrix_sync*. These primitives are executed by the 32 threads of a warp cooperatively. For FP16, the tile is further partitioned into 32 fragments while each thread fetches a fragment of data into its register files. Although the vendor’s official documents have not revealed the exact mapping schemes, existing works have figured them out through microbenchmarking [45], [48].

3.3 Cutlass Library

Currently the vendor’s high-performance linear-algebra library *cuBLAS* has not supported BMM on Turing tensorcores. However, their open-source GEMM library – *Cutlass* [31] has integrated it as an experimental and non-verified feature. BMM is realized using the WMMA API. The input matrix *A* is in row-major bit format (compacted as 32-bit unsigned int), *B* is in column-major bit format (also compacted as 32-bit unsigned int). The accumulated input matrix *C* and the result matrix *D* are in row-major 32-bit signed int format. *C* and *D* are usually the same matrix. BMM in *Cutlass* conducts 0/1 dot-product while BNN demands +1/-1 dot-product, we discuss this later.

4 BTC CHARACTERIZATION

To operate on the bit datatype for Turing GPUs, CUDA WMMA defines the 1-bit precision and the bit operations in an independent “*experimental*” namespace, as listed in Listing 1. XOR and POPC for bits (+1/-1) correspond to multiply and accumulate for floating-point/integer datatypes.

Five APIs are provided for loading the bit-tile *A*, the bit-tile *B*, the int-tile *C*, and storing the int-tile *D*, as well as the multiplication: $D = C + A \times B$. For the bit-matrix-multiply-API (BMMA), only a single computation paradigm is defined: the bit-tile *A* is in row-major of size (8, 128); the bit-tile *B* is in column-major of size (128, 8); the int-tile *C* and *D* are square matrices in row-/column-major of size (8, 8). The bit-tile *A* and *B* are compacted as 32 unsigned ints, each with 32 bits. Therefore, the bit-tile *A* and *B* each occupies 128 bytes. The int-tile *C* and *D* each occupies $8 \times 8 \times 4 = 256$ bytes. Listing 2 shows the *Parallel Thread Execution* (PTX) – the low-level GPU virtual machine ISA code for the five BMMA APIs. The shape qualifier “m8n8k128” in Line 2-6 indicate that the bit-tile-multiplication processed per warp is in size (8,128) \times (128,8) = (8,8). “sync” means the instruction wait for all warp lanes to synchronize before proceeding. The “layout” qualifier specifies if the tile is stored with a row-major or column-major order in memory. “type” indicates the precision of the tile. Using *int32* for tile-*C* and *D* is to avoid potential overflow during the accumulation.

For matrix-multiplication, tile-C and tile-D are usually in the same size. Thus, the five APIs can be categorized into three groups: *load*, *store*, and *computation*. We investigate each of them in the following subsection to figure out potential design guidelines. Regarding the hardware platform, see Section VII and Table 2.

4.1 BMMA Load

We first concentrate on *bmma_load*, as memory load is the most crucial factor for GEMM on GPU [55]. The load API is

```
1 void load_matrix_sync (fragment<...> &tileA, const T* mptr, unsigned ldm, layout_t layout);
```

It waits for all the threads of a warp to arrive, and then loads a bit tile (i.e., a matrix fragment) from the device memory. It has three parameters. "*mptr*" is a 256-bit aligned pointer pointing to the first element of the matrix in memory. The memory here can be global or shared memory. "*layout*" can be row- or column-major, but for BMMA, there is only a single choice — *mem_row_major* for matrix-A and *mem_col_major* for matrix-B. "*ldm*" is the stride in element between consecutive rows (in row major) or columns (in column major) and must be a multiple of 16 bytes), according to [56]. We find that for shared memory, this is the case; but for global memory, a multiple of 32 is also feasible (despite with unpredicted results). To see the impact of *mptr* (i.e., memory type) and *ldm* on the performance of the load primitive, we measure its average per-thread latency using the `clock()` instruction. We add a memory fence operation before the measurement to ensure that the data fetching has finished.

Figure 2, 3, 4, 5 show the average latency with respect to different values of *ldm* for *load_matrix_sync()* on global and shared memory of RTX-2080 and RTX-2080Ti GPUs. As *ldm* is the stride between consecutive rows of the matrix, it should be application dependent (e.g., for a $1024 \times 1024 \times 1024$ BMM, *ldm* should be 1024) and the raw latency should be irrelevant to *ldm*. However, counterintuitively it has a strong impact on the performance of fetching a bit-tile from the global memory. As can be seen in Figure 2 and Figure 4, *ldm*=128 and *ldm*=384 exhibit the shortest latency. Regarding shared memory, (1) accessing shared memory exhibits more than $5\times$ less latency than accessing global memory; (2) the latency for RTX2080Ti is less than RTX2080, and is unchanged with *ldm*.

We then consider "*tileA*", and see how the bit-tile (128×8 bits) is distributed among the lanes of a warp. Similar to [48], we let each lane print out the value of data it fetches. Based on the value, we can identify the mapping mechanism. We find that, similar to FP16 and Int8, lanes in BMMA also establish 8 thread groups — 4 consecutive lanes per group. Each thread group corresponds to a 128 bit row. Within a 128 bit row, each lane accounts for a 32-bit portion (4 bytes). This partially explains why *ldm*=128 delivers the shortest latency: the 32 lanes of the warp constitute a coalesced memory access, where the 32 4-byte access are merged as a single memory request. Regarding why *ldm*=384 also exhibits good performance, we suspect this might be because the Turing L1 data cache is essentially partitioned into two sectors with independent ports, similar to the L1/Tex cache in Maxwell and Pascal GPUs. It conserves the data in an interleaving way at a step of 32B. Consequently, *ldm*=256 (32B) may trigger a sector-port conflict for simultaneous memory fetches

from the same warp but *ldm*=384 may not. This is confirmed by the observation that *ldm*=128+256X (e.g., 384, 640, 896) all demonstrate relatively low latency in Figure 2 and 5.

4.2 BMMA Store

The store operation is different from load in that every element is a 32-bit signed integer. The store API is:

```
1 void store_matrix_sync (T* mptr, const fragment<...> &tileC, unsigned ldm, layout_t layout);
```

Again, it waits until all warp lanes arrived before storing *tileC* into memory. "*mptr*" must be a 256-bit aligned pointer referring to the first element. "*ldm*" describes the stride in elements between consequent rows in C, and must be a multiple of 16 bytes (with integer, it corresponds to 4 elements). "*layout*" can be row-major or column-major.

We measure the average latency with respect to the stride *ldm* on global and shared memory of RTX-2080 and RTX-2080Ti GPUs, as shown in Figure 6, 7, 8, 9, respectively. Unlike load, the latency histograms for store do not exhibit obvious patterns. We also attempt to figure out how the resulting int-tile *tileC* is distributed among the lanes. Our findings show that: (i) If it is row-major, then within the 8×8 int tile, each two consecutive elements (from a row) are stored in two adjacent registers of a lane. For example, suppose the 8×8 elements are E0 to E63 and each lane uses R4 and R5 to store the integer tile, then (E0, E1) are stored in R4 and R5 of lane-0, (E2, E3) are stored in R4 and R5 of lane-1, and so on. (ii) If it is column-major, then each two consecutive elements (from a column) are stored in two adjacent registers of a lane (i.e., transposed from the row-major layout). When storing, the two adjacent registers are encoded as one `STG.E.64` memory store for the entire warp, as if storing an FP64 data.

4.3 BMMA Computation

Finally, we discuss the bit-matrix-multiply API:

```
1 void bmma_sync(fragment<...> &tileD, const fragment<...> &tileA,
2 const fragment<...> &tileB, const fragment<...> &tileC,
3 experimental::bmmaBitOp=experimental::bmmaBitOpXOR,
4 experimental::bmmaAccumulateOp=experimental::bmmaAccumulateOpPOPC);
```

It waits until all lanes are available for conducting the BMMA operation: $\text{tileD} = \text{POPC}(\text{tileA} \text{ XOR } \text{tileB}) + \text{tileC}$. Unlike the condition for FP16 and Int8 where a group of SASS assembly operations are generated [45], [46], [48], *bmma_sync* is only translated into a single SASS code:

```
1 BMMMA.88128.XOR.POPC R2, R8.ROW, R9.COL, R2 ;
```

Our idea here is to measure its raw latency and estimate how much parallelism, including warp-level-parallelism (WLP) and instruction-level-parallelism (ILP), are required to saturate the tensorcore pipeline and hide the latency.

Figure 10, 11, 12, 13 illustrate the total latency of increasing the number of repeated *bmma_sync* operations for the same *tileC*/*tileD*, and different *tileC*/*tileD* on the two GPUs. The raw latency of *bmma_sync* is ~ 201 cycles on RTX2080 and ~ 190 cycles on RTX2080Ti. As shown in the figure, the incremental latency with each one more *bmma_sync* operation is 10 cycles when *tileC* & *tileD* are identical for all operations, and is 4 cycles when *tileC* & *tileD* are different on both platforms. This implies that the pipeline stage delay is around 4 cycles. When using the same accumulator, 6 extra

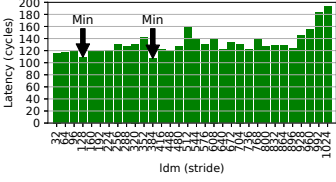


Fig. 2: RTX2080 global mem load

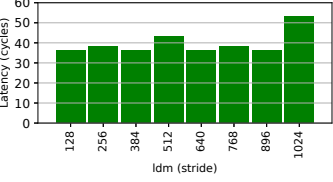


Fig. 3: RTX2080 shared mem load

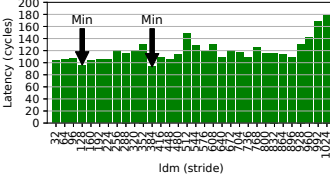


Fig. 4: RTX2080Ti global mem load

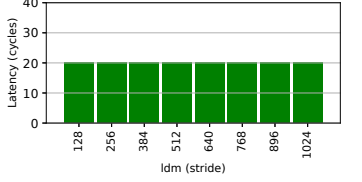


Fig. 5: RTX2080Ti shared mem load

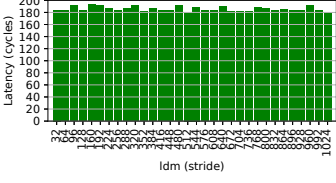


Fig. 6: RTX2080 global mem store

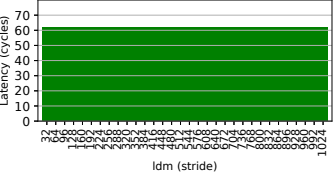


Fig. 7: RTX2080 shared mem store

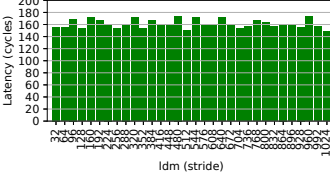


Fig. 8: RTX2080Ti global mem store

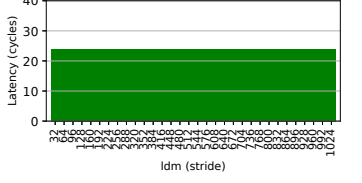


Fig. 9: RTX2080Ti shared mem store

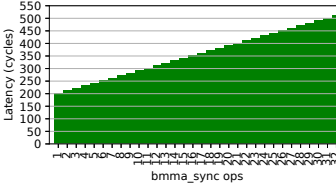


Fig. 10: RTX2080 bmma w/ same C

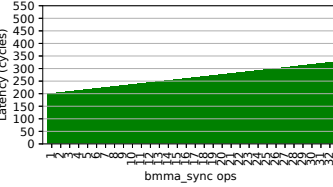


Fig. 11: RTX2080 bmma w/ diff C

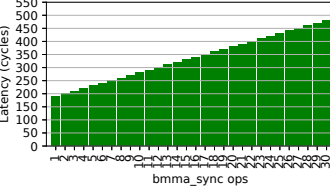


Fig. 12: RTX2080Ti bmma w/ same C

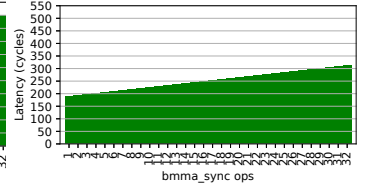


Fig. 13: RTX2080Ti bmma w/ diff C

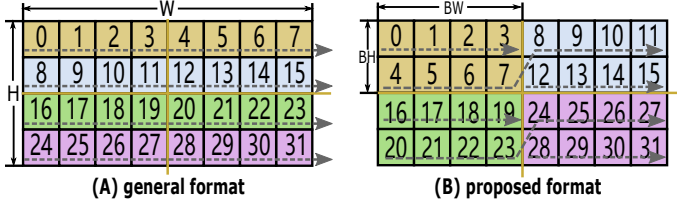
cycles are needed. Given the raw latency of ~ 200 cycles, and the fact that Turing GPU SM comprises four sub-cores (each subcore can issue one instruction per cycle), with at maximum 32 warps per SM for Turing (so $WLP=32$), we roughly require $ILP=200/4 \times 4/32 \approx 7$ to saturate the entire tensorcore pipeline. In other words, with 8 independent *bmma_sync* operations, we should approach the theoretical computation bandwidth of the tensorcores.

5 BMM AND BCONV WITH BTC

We present our designs for BTC-based BMM and BConv, which are the core functions for the fully-connected layer and convolution layer of BNNs.

5.1 FSB Data Format for BTC

In Section IV-A, we have observed that the value of *ldm* can strongly affect the performance of *load_matrix_sync* from global memory, where *ldm*=128 and 384 exhibit the best performance. Our idea thus is whether we can essentially fix the value of *ldm* firmly to 128 or 384. As a result, rather than storing the bits completely sequential and using the matrix width for *ldm*, as practiced by the *Cutlass* library and suggested by CUDA programming guide, we propose a new 2D bit data format where bits are stored in a unit of 128×8 bit-tile. An analogous example is shown in Figure 14. From the 1D general format to the 2D new format, an array of 8×4 bits ($H=4$, $W=8$) is converted with a tile size of 4×2 ($BH=2$, $BW=4$). For BTC, since 384 is not a power of 2, dividing 384 may incur troublesome remainder handling, we thus use 128 as BW and 8 as BH for the new format. If the original bits are organized in row-major, both the in-tile and tile-wise order of the new format are in row-major (as the case in Figure 14); otherwise, both are organized in column-major. Since the new format only changes the way how bits are stored and fetched, no extra space is needed. However, if the width of the original matrix (i.e., W) can

Fig. 14: Fixed-Stride-Bit (FSB) format based on a tile of $BH \times BW$.

not be divided by 128 (i.e., BW), for the convenience of index calculation, we pad the row to be a factor of 128, which may occupy some extra space. Note, in order to load via *load_matrix_sync()*, such a kind of padding is required anyway. Similar requirement has been imposed by *pitch* in *cudaMemcpy2D()*. The temporal overhead only occurs at array index calculation, which is almost negligible.

5.2 BMM for FC Layer

BMM in BNN is different from GEMM because: (a) *Input*. The elements of matrix-A and B are binary values: +1 and -1. A normal floating-point or int number is binarized via:

$$x^b = \text{sign}(x) = \begin{cases} 1 & \text{if } x \geq 0 \\ -1 & \text{otherwise} \end{cases} \quad (1)$$

In an FC layer, both A and B have to be binarized ahead of BMM. However, the binarization of B (i.e., weights) can be performed offline after the training; only the binarization of A is in the critical path of inference. Existing work has shown that such a binarization can be achieved efficiently through the `__ballot()` function of GPUs [26]; (b) *Computation*. The dot-product of GEMM is $y_{i,j} = \sum_{k=0}^{n-1} a_{i,k} b_{k,j}$ where n is the vector length. In terms of BMM, as a and b become bit-vectors, if using bit-1 to denote +1, and bit-0 to denote -1, it can be shown that the ± 1 dot-product becomes:

$$v = \vec{a} \cdot \vec{b} = n - 2 \times \text{popc}(\vec{a} \text{ xor } \vec{b}) = 2 \times \text{popc}(\vec{a} \text{ xnor } \vec{b}) - n \quad (2)$$

where n is the bit-vector length. *xor* and *xnor* are logical exclusive-or and exclusive-nor. The *xnor* expression has widely been used for BNN algorithm research [1], [3] and

```

1 __global__ void BMM(unsigned *A, unsigned *B, int *C, int A_height, int A_width, int B_width)
2 {
3     using namespace nvcc::wmma::experimental;
4     int bx = blockIdx.x * blockDim.x + threadIdx.x; int by = blockIdx.y;
5     wmma::fragment<wmma::matrix_a, 8, 8, 128, precision::b1, wmma::row_major> a_frag; //tile A
6     wmma::fragment<wmma::matrix_b, 8, 8, 128, precision::b1, wmma::col_major> b_frag; //tile B
7     wmma::fragment<wmma::accumulator, 8, 8, 128, int> c_frag; wmma::fill_fragment(c_frag, 0); //tile C
8     for (int i=0; i < (A_width/128); i++) {
9         load_matrix_sync(a_frag, A+bx*8-A_width/32+i*128/32, A_width); //fetch tile A
10        load_matrix_sync(b_frag, B+by*8-A_width/32+i*128/32, A_width); //fetch tile B
11        bmma_sync(c_frag, a_frag, b_frag, c_frag); //BMM
12        for (int i=0; i < c_frag.num_elements; i++) c_frag.x[i] = A_width - 2*c_frag.x[i]; //fix for +1/-1 logic
13        store_matrix_sync(C+(bx*8-B_width+by*8), c_frag, B_width, wmma::mem_row_major); //store tile C
14    }
15    BMM << < dim3(A_height/16, B_width/8), dim3(32, 2) >> (...); //invoke BMM kernel

```

Listing 3: BMM baseline implementation

```

1 __global__ void BMM(unsigned *A, unsigned *B, int *C, int A_height, int A_width, int B_width)
2 {
3     using namespace nvcc::wmma::experimental;
4     __shared__ uint4 As[32], Bs[32]; //buffering (8*128) 8 bit block in shared memory
5     const int laneid = threadIdx.x; const int wx = threadIdx.y; const int wy = threadIdx.z; //tile index
6     const int bx = blockIdx.x; const int by = blockIdx.y; //block index
7     wmma::fragment<wmma::matrix_a, 8, 8, 128, precision::b1, wmma::row_major> a_frag; //tile A
8     wmma::fragment<wmma::matrix_b, 8, 8, 128, precision::b1, wmma::col_major> b_frag; //tile B
9     wmma::fragment<wmma::accumulator, 8, 8, 128, int> c_frag; wmma::fill_fragment(c_frag, 0); //tile C
10    for (int k=0; k < A_width/32; k++) {
11        if (wx==0 && wy==0) { //one warp fetches data into shared memory for 16 warps of a thread block
12            As[laneid] = ((uint4*)A)[(bx*32+laneid)*A_width+k]; Bs[laneid] = ((uint4*)B)[(by*32+laneid)*B_width+k];
13        }
14        __syncthreads(); //for respecting RAW dependency
15        load_matrix_sync(a_frag, &As[wx*8], 128); load_matrix_sync(b_frag, &Bs[wy*8], 128);
16        bmma_sync(c_frag, a_frag, b_frag, c_frag);
17        __syncthreads(); //for respecting WAR dependency
18        for (int i=0; i < c_frag.num_elements; i++) c_frag.x[i] = (A_width/128) - (2*c_frag.x[i]); //+1/-1 BMM
19        store_matrix_sync(C+((bx*4+wx)*8-B_width+(by*4+wy)*8), c_frag, B_width, wmma::mem_row_major);
20    }
21    BMM << < dim3(A_height/32, B_width/32), dim3(32, 4) >> (...);

```

Listing 4: Bit-Matrix-Multiplication

FPGA/ASIC implementation [20], [21] while GPU tensor-cores currently only support *xor* for BMM computation. *popc* stands for population count, which counts the number of bit-1s in the bit vector. (c) *Output*. The elements of the output matrix-C are full-precision integer values. However, in an FC layer, it can be binarized after a threshold operation (discussed later), reducing memory access. Therefore, the third difference with GEMM is that the output-C can be binarized before the store.

Design-1 Now we present our three BMM designs based on WMMA, which is the only API for operating the tensor-cores. The baseline design is shown in Listing 3. Each thread block comprises two warps and each warp processes BMM for a 128×8 bit-tile in Line 10. Having two warps per thread block is for achieving the full occupancy of Turing SMs.

Design-2 As memory load is the most important factor for matrix multiplication on GPU [55], Design-2 aims at improving the efficiency of memory load. On one hand, using a whole warp to fetch only 128 bits is too lightweight. On the other hand, if coalescing memory access is enforced with each lane fetches 32bits, the total bit length becomes $32 \times 4 \times 8 = 1024$ bits, which is probably too coarse-grained for a BNN FC layer given the matrix size is usually less than 2048. Therefore, motivated by [45], we increase the load granularity per warp-lane to its max value of 128 bits, leveraging the effective LDG.E.128 SASS instruction. With each lane fetching 128 bits, a warp of 32 lanes would fetch a bit segment of 4096 bits, which is sufficient for 4 warps to perform WMMA simultaneously. As a result, we use a representative warp to fetch 4096 bits of A and 4096 bits of B from global memory to shared memory, which are then dispatched to 16 warps for WMMA execution, as listed in Listing 4. Essentially, each thread block processes a BMM of $(128, 32) \times (32, 128)$ while each warp processes $(128, 8) \times (8, 128)$. Line 11-12 show how to invoke 128-bit global memory load through vectorization [45]. Note that

```

1 #define FLIPBITS(n,b) ((n)^(1u<<(b)-1)) //flip the last b bits of n
2 __global__ void BMMb(unsigned *A, unsigned *B, unsigned *C, int A_height, int A_width, int B_width)
3 {
4     using namespace nvcc::wmma::experimental;
5     int bx = blockIdx.x * blockDim.x + threadIdx.x; int by = blockIdx.y;
6     __shared__ int Cs[64];
7     unsigned laneid; asm("mov.u32 %0, %%laneid;": "r" (laneid)); //get laneid
8     wmma::fragment<wmma::matrix_a, 8, 8, 128, precision::b1, wmma::row_major> a_frag; //tile A
9     wmma::fragment<wmma::matrix_b, 8, 8, 128, precision::b1, wmma::col_major> b_frag; //tile B
10    wmma::fragment<wmma::accumulator, 8, 8, 128, int> c_frag; wmma::fill_fragment(c_frag, 0); //tile C
11    for (int i=0; i < (A_width/128); i++) {
12        load_matrix_sync(a_frag, A+bx*8-A_width/32+i*128/32, A_width); //fetch tile A
13        load_matrix_sync(b_frag, B+by*8-A_width/32+i*128/32, A_width); //fetch tile B
14        bmma_sync(c_frag, a_frag, b_frag, c_frag); //BMM
15        for (int i=0; i < c_frag.num_elements; i++) c_frag.x[i] = A_width - 2*c_frag.x[i]; //fix for +1/-1 logic
16        store_matrix_sync(Cs, c_frag, B_width, wmma::mem_row_major); //store tile C
17        union { unsigned data; uchar elements[4]; } p0, p1;
18        p0.data = __ballot(A_width - 2*Cs[laneid] >= 0);
19        p1.data = __ballot(A_width - 2*Cs[laneid+32] >= 0);
20        if ((laneid < 4) && (uchar) Cb = (uchar) C[0];
21        Cb[(bx*8+laneid)*(B_width/8)+FLIPBITS(by,2)] = p0.elements[3] - laneid;
22        Cb[(bx*8+4+laneid)*(B_width/8)+FLIPBITS(by,2)] = p1.elements[3] - laneid; }
23    }
24    BMMb << < dim3(A_height/16, B_width/8), dim3(32, 2) >> (...); //invoke BMMb kernel

```

Listing 5: BMM in new format with binarized output

```

1 __global__ void BTC_Conv2d(const unsigned* __restrict__ input,
2                          const unsigned* __restrict__ filter, int* output, const int in_channels, const int out_channels,
3                          const int in_width, const int in_height, const int filter_width, const int filter_height,
4                          const int batch, const int stride_vertical, const int stride_horizontal, const int out_width,
5                          const int out_height, const int pad_h, const int pad_w)
6 {
7     using namespace nvcc::wmma::experimental;
8     wmma::fragment<wmma::matrix_a, 8, 8, 128, precision::b1, wmma::row_major> a_frag;
9     wmma::fragment<wmma::matrix_b, 8, 8, 128, precision::b1, wmma::col_major> b_frag;
10    wmma::fragment<wmma::accumulator, 8, 8, 128, int> c_frag;
11    unsigned laneid; asm("mov.u32 %0, %%laneid;": "r" (laneid)); //get laneid
12    const int bx = blockIdx.x; //over O: out_width
13    const int by = blockIdx.y; //over P: out_height
14    const int bz = blockIdx.z; //over C: out_channel/8 + batch/8
15    const int ins = (in_channels > 7); //number of steps in C: in_channels
16    const int bn = bz/(out_channels > 3); //batch
17    const int bo = bz%(out_channels > 3); //out_channel
18    //coord (ax,ay) in input from bx,by in Output
19    const int ax0 = bx*stride_horizontal - pad_w; const int ay0 = by*stride_vertical - pad_h;
20    //track the number of filter entries that are masked off
21    int exclude = 0; wmma::fill_fragment(c_frag, 0);
22    //load a window of data from input
23    for (int r=0; r < filter_height; r++) {
24        for (int s=0; s < filter_width; s++) {
25            const int ay = ay0 + r; //y - coord in input
26            const int ax = ax0 + s; //x - coord in input
27            if ((ay >= 0) && (ay < in_height) && (ax >= 0) && (ax < in_width)) { //within input frame
28                for (int c=0; c < ins; c++) { //per 128-bit in C: in_channels
29                    //input: [H,W,N,C], filter: [K,K,O,C]
30                    load_matrix_sync(a_frag, &input[(ay-in_width+ax)*batch+ins+4+bn-ins-32+c*4], in_channels);
31                    load_matrix_sync(b_frag, &filter[(r-filter_width+s)*out_channels+ins+4+bo-ins-32+c*4], in_channels);
32                    bmma_sync(c_frag, a_frag, b_frag, c_frag);
33                }
34            }
35            else exclude++; //accumulate for points not in frame
36        }
37    }
38    for (int i=0; i < c_frag.num_elements; i++)
39        c_frag.x[i] = in_channels-filter_height-filter_width - exclude-in_channels - (2*c_frag.x[i]);
40    //output: [P,Q,N,O] => [by,bx,bn,bo]
41    store_matrix_sync(&output[(by-out_width+bx)*batch-out_channels+bn*8-out_channels+bo*8],
42                    c_frag, out_channels, wmma::mem_row_major);
43 }

```

Listing 6: BTC-based BConv design

load_matrix_sync is $5 \times$ faster on shared memory than global memory (Section IV-A).

Design-3 We adopt our new FSB format for BMM. Listing 5 shows the design with the output matrix binarized. As can be seen, after BMM, each warp holds a tile of C in size of 8×8 . We use `__ballot()` to binarize the 64 elements using the entire 32 lanes in Line 17-18. In order to write an 8-bit uchar to a 32-bit unsigned, we define a union for packing and unpacking. As NVIDIA GPUs adopt little endian, we define `FLIPBIT()` for efficient byte index translation.

5.3 BConv for Convolution Layer

The convolution operation here is to cross-correlate a 4D input tensor (*batch*, *input_height*, *input_width*, *input_channels*) with a 4D weight tensor (*weight_height*, *weight_width*, *input_channels*, *output_channels*). We use H to denote input_height, W to denote input_width, N to denote batch, C to denote input_channel, K to denote weight size and O to denote output_channel. *TensorFlow* thus uses NHWC for input and KKCO for filter. *PyTorch* uses NCHW for input and OCKK for filter. Traditionally, a 2D convolution can be transformed

into GEMM through the *im2col()* process [28], [29], which can then be accelerated by the tensorcores. However, for BConv, directly converting to BMM is not feasible due to the challenge in padding [30]. Different from normal convolution where the padded zeros shall not affect the correctness, in BConv the element zero actually denotes -1. Therefore, after the *im2col()* process, we are unable to distinguish the padded 0s from the meaningful zeros representing -1, leading to inaccurate results.

Thus, the objective here is how to design BConv so that the padding issue can be well-managed but can still be accelerated by the bit tensorcores of Turing GPUs. On one hand, motivated by existing work [26], if the entire filter window is processed sequentially by a single GPU thread, a status variable can be allocated to track how many entries of the filter window fall out of the frame of the input image, which can be used later to make an amendment accordingly for ensuring the correctness of bit-padding. On the other hand, if we ignore the image size and filter size for now but looking at a particular point $[i,j]$ of the input image, the batch of N images at that point cross-correlating with an entry of the filter window $[r,s]$ is essentially to calculate the following output point $[p,q]$:

$$Output_{[p,q]} = \sum_{k=1}^C input(N, k)_{[i,j]} \times filter(k, O)_{[r,s]} \quad (3)$$

This is just equivalent to multiplying a bit matrix in size (N, C) with another matrix in size (C, O) , which can be performed by the bit-tensorcores. To summarize, our idea is to change the input tensor to *HWNC*, the filter tensor to *KKCO*, and perform BMM along the last two dimensions of these two tensors.

Our first design is shown in Listing 6. We use each warp to traverse the *input_channel* space at Line 28 and perform the computation for 8 *input_images* over 8 *output_channels* (i.e., $(8, C) \times (C, 8)$) using the bit-tensorcores in Line 30-32. We use "exclude" to track the number of entries outside the filter frame at Line 33 and amendment the results at Line 36 for padding and the ± 1 logic (see Eq 2). We use *c_frag* for storing the partial results of convolution. Eventually, the 8×8 resulting matrix tile stored in *c_frag* is written back to the global memory in row-major at Line 38-39.

Our second BConv design leverages the new bit data format. We reform the last two dimensions of the input tensor (N, C) in a bit-tile of 128×8 bits in row-major, and the filter tensor (C, O) in a bit-tile of 128×8 bits in column-major. Then, we can adjust the *ldm* in Line 30-31 from "in_channels" to 128, later we will show the impact of this adjustment.

6 BNN DESIGN WITH BTC

We present the overall BNN structure and our BTC-based BNN implementation.

6.1 BNN Network Structure

Figure 15 illustrates the network structure of an example ResNet. To avoid losing too much non-recoverable information at the beginning, if the input images are in full-precision (e.g., after preprocessing), the first layer of BNN is not binarized [2], [3], [7]. BWN is adopted here in which only the weight matrix is binarized. Consequently, we are

unable to use BTC to accelerate the first layer. Also because the input channels of the first layer is usually very small (e.g., red, green, blue), to avoid alignment issue and fully leverage data locality, we binarized the weight matrix into a 4D bit tensor in *KKCO* format and buffer the weight into the shared memory for reuse. Then, by extracting each bit of the weight, depending on whether it is 1 or 0, we add or subtract the corresponding element of the input matrix. The output matrix is binarized and stored in particular bit-format as the input for the next layer.

Shown in Figure 15, regarding training, a BNN convolution layer typically comprises *binarization* (*sign*), *bit-convolution* (*conv*), *batch-normalization* (*bn*), *hard-tanh* (*tanh*), and *pooling* (*pool*). Binarization is the *sign* function following Eq 1. Batch-normalization [57] is to reduce the batch noise:

$$y_{i,j} = \left(\frac{x_{i,j} - \mathbb{E}[x_{*,j}]}{\sqrt{\text{Var}[x_{*,j}] + \epsilon}} \right) \cdot \gamma_j + \beta_j \quad (4)$$

Note that *bn* is essential for BNNs, as missing it will render the training unable to converge. Additionally, having *bn* brings two extra benefits: (1) bias is thus not necessary for the bit convolution or fully-connected layer, as bias can be integrated with β_j in Eq 4; (2) the scaling layer proposed in [3], [7] for BNN is also not necessary as it can be integrated with γ_j in Eq 4. Hard *tanh* is a piecewise linear function:

$$Htanh(x) = Clip(x, -1, 1) \quad (5)$$

Since *tanh* is immediately followed by the *sign* function, it has none effect on inference or the forward pass of training. The major purpose of *tanh* is to constrain the gradient of the *sign* function between -1 and +1 in the backward pass [1]. Otherwise, if the full-precision activation is too large, the gradient will be zeroed-out. Additionally, since the *sign* binarization function has already imposed non-linearity into the network, no other activation function such as *ReLU* [3] and *PRelu* [7] is actually needed for BNN. Conversely, extra activation functions can be harmful based on our tests.

Regarding the order of these functions, it should be *tanh*→*sign*→*bconv*→*pool*→*bn*→*tanh*→*sign* for the training, as it has already been shown that placing *pool* before *bn* can lead to increased training accuracy [3], [30]. However, for inference it would be much faster if equivalently *pool* is located after *bn* and even the binarization of the next layer to convert a max pooling into a logic-OR operation [21], [26]. Additionally, for inference, *bn* and *sign* of the next layer can be aggregated as a simple threshold comparison operation (i.e., returns +1 if greater than a threshold τ and -1 otherwise) [21], [26], labeled as *thrd* in Figure 15. In this way, *thrd* can be further fused with *bconv* or *bmm* to reduce the volume of data access if the residual is not saved. Finally, *tanh* is not required for inference as discussed. Consequently, the ultimate function order becomes *thrd*→*bconv*→*thrd*→*pool*→*bconv* for inference. Similar condition is also applied for the FC layers.

Traditionally, the last layer of BNN is also in full-precision [1], [3]. However, Tang et al. [7] showed that binarizing the final layer with a learned scaling layer could significantly compact the model as FC layers comprises the most parameters. Our observation here is that such a scaling layer can be absorbed by adding a *bn* function for the last layer, which may provide even better performance due to

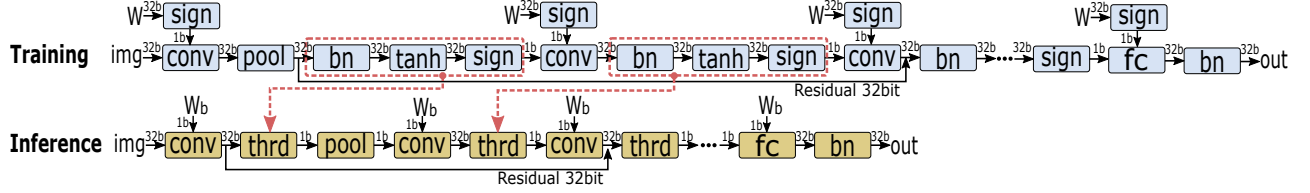


Fig. 15: A typical network structure of a ResNet BNN including 3 Conv layers and 1 FC layer for training and inference.

more constraint output range for the following softmax function. Note, for the final layer, since the output is real-valued and there is no future binarization, *bn* cannot be converted into a *thrd* function.

In terms of more advanced models such as ResNet, to avoid gradient diminishing or explosion, the cross-layer shortcut connections become vital. Here, the main performance concern is that these residuals are real-valued (bit-residual cannot convey gradient), which may incur substantial extra memory load & store compared with directly saving the bits after *thrd*. In addition, the residual may need a pooling layer before the injection. Furthermore, it is also possible that the number of channels needs to adjust. In those scenarios, we use the type-A shortcut of ResNet [58].

6.2 BTC based Implementation

Similar to [26], we have also fused all the layer functions into a single GPU kernel so the repeated kernel invocation & release overhead (as long as 20 μs per invocation [59]) can be eliminated. We implement each layer function as a GPU device function. These device functions are called from a global function where the BNN network model is defined. Due to data dependency across the layers, to ensure consistency, we rely on CUDA’s cooperative-groups for global synchronization among all SMs. There are two major challenges for the overall design here: (i) *Achieving high SM utilization*. Since WMMA is executed at the warp level, with 32 warps per SM for Turing GPUs and 68 SMs in RTX2080Ti for instance, the overall parallelism offered by the hardware is 2176 warps, implying 2176 BMMs sized $(8,128) \times (128,8)$ per round. Consequently, the task granularity per warp should be as small as possible in order to use all the SM warp slots and achieve workload balance; (ii) *Adapting to WMMA format*. As BTC can only process BMM sized $(8,128) \times (128,8) = (8,8)$, we need to ensure the row of the FC input matrix, the column of the weight, the batch of the BConv image, and the output channel can all divide 8, while the column of the FC input matrix, the row of the weight, the input channel of BConv can all divide 128. Both requirements need to be consistent across all layers. Given the BNN model can be in arbitrary configuration and we internally use our own FSB format, the address translation and calculation become more complicated. There is another format change after the final Conv layer and ahead of the first FC layer to ensure correct format transition.

7 EVALUATION

We evaluate our BTC-based BNN design in this section. We first describe the experiment configurations. Then, we show the evaluation results for BMM and BConv. Finally, we discuss the performance of BNN using different models and datasets.

7.1 Experiment Configuration

We use two NVIDIA Turing GPUs with CC-7.5 for evaluation. Their information is listed in Table 2. The RTX2080 GPU is in a Linux 3.10.0 system with Intel Xeon E5-2680 CPU at 2.80 GHz, 128 GB DDR3 DRAM and gcc-4.8.5. The RTX2080Ti GPU is in a Linux 2.6.32 system with Intel Xeon E5-6230 CPU at 2.10 GHz, 384 GB DDR4 DRAM and gcc-4.8.5. All the results reported are the average of 10 times’ execution.

7.2 BMM Evaluation

For BMM evaluation, we randomly generate square matrices with increased sizes from 128 until 16K. We use the full-precision GEMM from *cuBLAS* as the baseline for validation and performance comparison. We compare our three BTC-based BMM designs with the BMM approach from [3], the four BSTC BMM designs from [26], and the BTC uint-4 and BMM designs from *Cutlass* [31]. We conduct two types of testing: (1) **General BMM** where both the input matrices and the output matrix are floating-points. It includes binarization for A and B, but excludes the binarization for C. The tested schemes are listed in Table 3. (2) **BNN-specific BMM** where both the input matrices and the output matrix are binarized. It includes binarization for C but excludes A and B. This test reflects how BMM actually behaves in a BNN FC layer. The schemes are listed in Table 4.

Figure 16, 17, 18 and 19 show the results of the two BMM tests on TU104 RTX2080 GPU and TU102 RTX2080Ti GPU, respectively. For general BMM in Figure 16 and 18, we have three major observations: (I) No single approach dominates the entire matrix range — For small matrices ($n \leq 1K$), the fine-grained 64bit BSTC is relatively better although the advantage is marginal. This might be due to more fine-grained thread-block tasks to leverage all SMs; For medium matrices ($1K < n \leq 4K$), Design-3 based on the proposed FSB-format obtains the best performance, particularly at 4K. For large matrices ($n > 4K$), the performance of all BTC based designs drop. This is due to the fierce competition in BTC and reduced data reuse in the L0/L1 cache. Nevertheless, the size of FC layers of most BMMs fall in the medium range. (II) Comparing among Design-1, 2, and 3, while Design-2 is always better than Design-1 due to improved load efficiency and shared memory reuse, the new-format based Design-3 significantly outperforms Design-1/2 except on very large matrices. Overall, without this new FSB format, BTC may not deliver any performance advantage over existing BSTC software solutions. For BNN-specific BMM in Figure 17 and 19, the avoidance of binarizing A & B, and reduced memory store after binarizing C, dramatically amplify the supremacy of Design-3. The speedup is more than $20\times$ over the full-precision *cuBLAS* at 4K on RTX2080. (III) Comparing between BMMs and uint-4 based GEMM over the same TCUs,

TABLE 2: Evaluation Platforms. "Reg" refers to the number of 4-byte registers. "Thds" refer to threads. "Dri/Rtm" refer to CUDA driver and runtime versions.

| GPU | Arch/CC | Code | SMs | CTAs/SM | Warps/SM | Thds/CTA | Regs/SM | Shared/SM | TCUs/SM | Memory | Mem Bandwidth | Dri/Rtm |
|------------|------------|-------|-----|---------|----------|----------|---------|-----------|---------|------------|---------------|-----------|
| RTX-2080Ti | Turing-7.5 | TU102 | 68 | 16 | 32 | 1024 | 64K | 64K | 8 | 11GB GDDR6 | 616 GB/s | 10.1/10.0 |
| RTX-2080 | Turing-7.5 | TU104 | 46 | 16 | 32 | 1024 | 64K | 64K | 8 | 8GB GDDR6 | 448 GB/s | 10.0/10.0 |

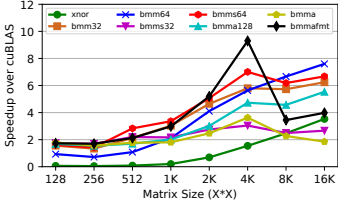


Fig. 16: General BMM on RTX2080

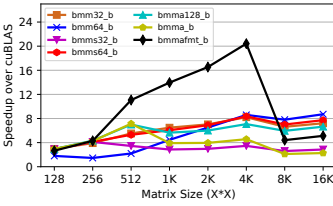


Fig. 17: Specific BMM on RTX2080

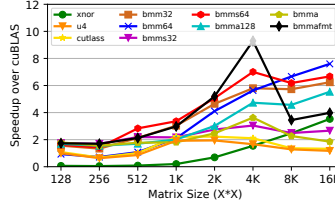


Fig. 18: General BMM on RTX2080Ti

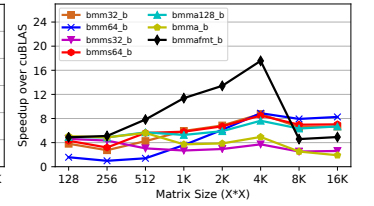


Fig. 19: Specific BMM on RTX2080Ti

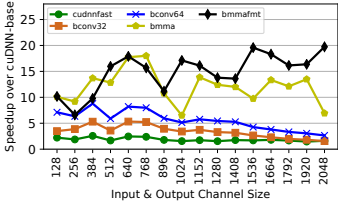


Fig. 20: General BConv on RTX2080

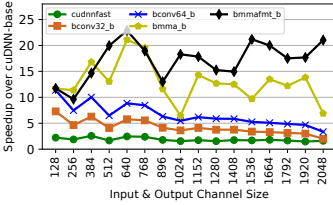


Fig. 21: Specific BConv on RTX2080

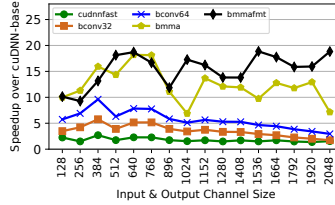


Fig. 22: General BConv on RTX2080Ti

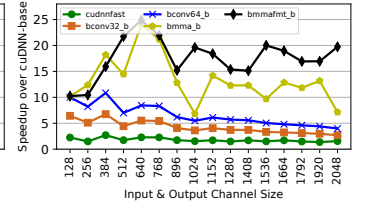


Fig. 23: Specific BConv on RTX2080Ti

TABLE 3: BMM full-precision output schemes.

| Schemes | Description | Algorithm | Input | Output |
|---------|---|-----------|-------|--------|
| cuBLAS | Simulating BMM via SGEMM | SGEMM | 32bit | 32bit |
| xnor | BMM design in [1] | BMM | 32bit | 32bit |
| bmm32 | 32bit BSTC BMM in [26] | BMM | 32bit | 32bit |
| bmm64 | 64bit BSTC BMM in [26] | BMM | 32bit | 32bit |
| bmm32 | Fine-grained 32bit BSTC BMM in [26] | BMM | 32bit | 32bit |
| bmm64 | Fine-grained 64bit BSTC BMM in [26] | BMM | 32bit | 32bit |
| cutlass | BTC BMM in Cutlass library [31] | BMM | 1bit | 32bit |
| u4 | BMM via unsigned 4-bits MM [31] | 4bits-MM | 4bit | 32bit |
| bmma | Design-1: basic BTC implementation | BMM | 32bit | 32bit |
| bmma128 | Design-2: 128bit load and shared memory | BMM | 32bit | 32bit |
| bmmafnt | Design-3: new format | BMM | 32bit | 32bit |

TABLE 4: BMM bit output schemes.

| Schemes | Description | Input | Output |
|-----------|---|-------|--------|
| bmm32_b | 32bit BSTC BMM in [26] with bin output | 1bit | 1bit |
| bmm64_b | 32bit BSTC BMM in [26] with bin output | 1bit | 1bit |
| bmm32_b | Fine-grained 32bit BSTC BMM in [26] with bin output | 1bit | 1bit |
| bmm64_b | Fine-grained 64bit BSTC BMM in [26] with bin output | 1bit | 1bit |
| bmma_b | Design-1: basic BTC implementation with bin output | 1bit | 1bit |
| bmma128_b | Design-2: 128bit load with bin output | 1bit | 1bit |
| bmmafnt_b | Design-3: new format with bin output | 1bit | 1bit |

we can observe that BMMs demonstrate obvious advantage. This is largely because (a) the smaller memory footprint (1-bit vs 4-bits) reduces the bandwidth and storage pressure over the data-path and registers; (b) with the same bit-width for the ALUs in the TCUs, using 1-bit can compact $4\times$ more data elements than using int-4 or uint-4. Similar conditions apply to other types such as int-8 and FP16.

7.3 BConv Evaluation

For BConv, there are much more parameters than BMM: *input_height*, *input_width*, *weight_height*, *weight_width*, *batch*, *input_channels*, *output_channels*, *stride*, *pooling*, etc. We compare our two BTC-based designs (Note that we use *bmma* to denote Design-1 and *bmmafnt* to denote Design-2) with full-precision *cuDNN-base* (no workspace), *cuDNN-fast* (plenty workspace), and two BSTC designs (*bconv32* and *bconv64*) from [26]. We use *cuDNN-base* as the baseline and perform the two types of test: (1) **General BConv** where the input, filter and output tensors are all floating-points; (2) **BNN-specific BConv** where all of them are binarized.

Figure 20, 21, 22 and 23 show the results of the two types of tests with *batch*=16, *input_size*=64, *weight_height*=3

and *stride*=1 on the two GPUs. We increase both *input_channels* (C) and *output_channels* (O) from 128 to 2048. As is shown, our two BTC-based approaches exhibit considerable speedups over existing methods. Particularly, the FSB new format design achieves about $25\times$ over the full-precision *cuDNN* with C=O=640 on RTX2080Ti. Comparing between the two BTC designs, we can see that (i) when C=O=128, the two designs are just equivalent, so they show similar performance; (ii) When C=O=384, Design-1 is better possibly because *ldm*=384 is also a good choice for memory load (see Section IV). (iii) For the other points, Design-2 shows obvious advantages.

7.4 BNN Evaluation

Finally, we evaluate the overall BNN implementation. Table 5 lists the six models we used for evaluation. Table 6 and 7 list the latency and throughput we obtained for the six models on the two NVIDIA Turing GPUs, respectively. The latency is measured under a batch size of 8 since 8 is the smallest value to leverage the bit-tensorcores so essentially the latency is for the inference of 8 images. The throughput is measured under a batch of 1024 images for *MNIST* and *Cifar10*, and 512 for *ImageNet*. We compare our performance with the four approaches from the latest BSTC SBNN work (from <http://github.com/uuudown/SBNN>) [26]. Overall, compared with the best approach *SBNN-64-Fine* from SBNN, our BTC using the default format design achieves on average $2.10\times$ in latency and $1.65\times$ in throughput on RTX2080Ti, and $2.08\times$ in latency and $1.62\times$ in throughput on RTX2080 across the six models. Our proposed BTC new format achieves $2.33\times$ in latency and $1.81\times$ in throughput on RTX2080Ti, and $2.25\times$ in latency and $1.77\times$ in throughput on RTX2080. The best speedup has been achieved by the FSB-format based design on RTX2080Ti for ResNet-14 on *Cifar10* — $3.79\times$ in latency and $2.84\times$ in throughput.

Regarding this result, we have three observations: (I) Our BTC design generally achieves more than $2\times$ over existing work except for *MNIST-MLP* and *ImageNet-Alexnet* where the throughput is actually a little bit worse. The reason is

TABLE 5: BTC Evaluation. “1024FC” refers to a fully-connected layer with 1024 neurons. “2x128C3” refers to 2 convolution layer with 128 output channels and 3x3 filter. “P2” refers to a 2x2 pooling layer. “128C11/4” refers to a convolution layer with 128 output channels, 11x11 filter size and stride=4. “Input size” is of $input_height \times input_width \times input_channels$ format. “Output” is the number of categories to classify. “Ref” is short for references. “BNN” refers to state-of-the-art BNN training accuracy from existing work. “Our BNN” is the BNN training accuracy we obtained from our own BNN implementation. “Full-Precision” is the 32 bits full-precision training accuracy from existing works.

| Dataset | Ref | Network | Ref | Network Structure | Input Size | Out | BNN | Our BNN | Full-Precision |
|----------|------|-----------|------|---|------------|------|----------------|------------|----------------|
| MNIST | [60] | MLP | [1] | 1024FC-1024FC-1024FC-1024FC | 28x28x1 | 10 | 98.6% [1] | 97.6% | 99.1% [1] |
| Cifar-10 | [61] | VGG | [4] | (2x128C3)-MP2-(2x256C3)-MP2-(2x512C3)-MP2-(3x1024FC) | 32x32x3 | 10 | 89.9% [1] | 88.7% | 90.9% [8] |
| Cifar-10 | [61] | ResNet-14 | [3] | 128C3/2-4x128C3-4x256C3-4x512C3-(2x512FC) | 32x32x3 | 10 | N/A | 91.6% | N/A |
| ImageNet | [62] | AlexNet | [63] | (128C11/4)-P2-(256C5)-P2-(3x256C3)-P2-(3x4096FC) | 224x224x3 | 1000 | 75.7/46.1% [8] | 74.2/44.7% | 80.2/56.6% [8] |
| ImageNet | [62] | VGG-16 | [64] | (2x64C3)-P2-(2x128C3)-P2-(3x256C3)-P2-2x(3x512C3)-P2-(3x4096FC) | 224x224x3 | 1000 | 76.8%/NA [41] | 77.7/53.4% | 88.4%/NA [41] |
| ImageNet | [62] | ResNet-18 | [3] | 64C7/4-4x64C3-4x128C3-4x256C3-4x512C3-(2x512FC) | 224x224x3 | 1000 | 73.2/51.2% [3] | 72.7/48.6% | 89.2/69.3% [3] |

TABLE 6: BTC Inference Performance on NVIDIA Turing RTX2080 GPU.

| | MNIST-MLP | | Cifar10-VGG | | Cifar10-ResNet14 | | ImageNet-AlexNet | | ImageNet-VGG | | ImageNet-ResNet18 | |
|--------------|-----------|------------------------|-------------|------------------------|------------------|------------------------|------------------|------------------------|--------------|------------------------|-------------------|------------------------|
| Schemes | 8 Latency | Throughput | 8 Latency | Throughput | 8 Latency | Throughput | 8 Latency | Throughput | 8 Latency | Throughput | 8 Latency | Throughput |
| SBNN-32 | 0.227ms | 2.88×10^6 fps | 1.891ms | 1.06×10^4 fps | 5.138ms | 4.17×10^3 fps | 4.494ms | 3.18×10^3 fps | 27.638ms | 4.26×10^2 fps | 6.550ms | 2.60×10^3 fps |
| SBNN-32-Fine | 0.082ms | 1.97×10^6 fps | 1.536ms | 1.05×10^4 fps | 4.382ms | 3.97×10^3 fps | 3.928ms | 3.05×10^3 fps | 27.009ms | 4.25×10^2 fps | 5.944ms | 2.37×10^3 fps |
| SBNN-64 | 0.908ms | 8.44×10^4 fps | 2.816ms | 1.06×10^4 fps | 8.132ms | 4.59×10^3 fps | 17.258ms | 1.95×10^3 fps | 40.247ms | 5.23×10^2 fps | 8.108ms | 3.01×10^3 fps |
| SBNN-64-Fine | 0.074ms | 5.51×10^6 fps | 0.999ms | 1.63×10^4 fps | 2.550ms | 6.52×10^3 fps | 2.871ms | 3.79×10^3 fps | 16.68ms | 6.65×10^2 fps | 3.736ms | 3.42×10^3 fps |
| BTC | 0.061ms | 3.37×10^6 fps | 0.364ms | 3.62×10^4 fps | 0.827ms | 1.58×10^4 fps | 2.367ms | 3.85×10^3 fps | 7.449ms | 1.24×10^3 fps | 1.869ms | 5.48×10^3 fps |
| BTC-FMT | 0.055ms | 5.48×10^6 fps | 0.338ms | 3.85×10^4 fps | 0.724ms | 1.71×10^4 fps | 2.326ms | 3.77×10^3 fps | 7.021ms | 1.34×10^3 fps | 1.833ms | 5.55×10^3 fps |

TABLE 7: BTC Inference Performance on NVIDIA Turing RTX2080Ti GPU.

| | MNIST-MLP | | Cifar10-VGG | | Cifar10-ResNet14 | | ImageNet-AlexNet | | ImageNet-VGG | | ImageNet-ResNet18 | |
|--------------|-----------|------------------------|-------------|------------------------|------------------|------------------------|------------------|------------------------|--------------|------------------------|-------------------|------------------------|
| Schemes | 8 Latency | Throughput | 8 Latency | Throughput | 8 Latency | Throughput | 8 Latency | Throughput | 8 Latency | Throughput | 8 Latency | Throughput |
| SBNN-32 | 0.252ms | 2.99×10^6 fps | 1.596ms | 1.19×10^4 fps | 4.909ms | 4.68×10^3 fps | 1.937ms | 7.62×10^3 fps | 23.788ms | 5.13×10^2 fps | 5.863ms | 3.08×10^3 fps |
| SBNN-32-Fine | 0.082ms | 2.43×10^6 fps | 1.548ms | 1.19×10^4 fps | 4.061ms | 4.65×10^3 fps | 1.733ms | 7.16×10^3 fps | 22.722ms | 5.06×10^2 fps | 5.145ms | 3.10×10^3 fps |
| SBNN-64 | 0.952ms | 1.03×10^6 fps | 2.921ms | 1.37×10^4 fps | 8.633ms | 5.95×10^3 fps | 14.214ms | 2.59×10^3 fps | 31.561ms | 7.08×10^2 fps | 8.092ms | 3.91×10^3 fps |
| SBNN-64-Fine | 0.070ms | 6.87×10^6 fps | 0.926ms | 2.09×10^4 fps | 2.341ms | 7.86×10^3 fps | 2.017ms | 4.99×10^3 fps | 12.057ms | 8.83×10^2 fps | 3.233ms | 4.52×10^3 fps |
| BTC | 0.057ms | 4.38×10^6 fps | 0.317ms | 4.69×10^4 fps | 0.728ms | 2.06×10^4 fps | 1.878ms | 4.87×10^3 fps | 5.840ms | 1.62×10^3 fps | 1.538ms | 7.23×10^3 fps |
| BTC-FMT | 0.053ms | 6.78×10^6 fps | 0.276ms | 5.06×10^4 fps | 0.618ms | 2.24×10^4 fps | 1.862ms | 4.87×10^3 fps | 5.466ms | 1.76×10^3 fps | 1.438ms | 7.34×10^3 fps |

TABLE 8: Comparing with FPGA works using AlexNet on ImageNet.

| AlexNet/ImageNet | Platform | Raw Latency | Throughput |
|------------------|---------------------------|--------------|------------|
| RebNet [65] | Xilinx Virtex VCU108 FPGA | 1902 μ s | 521 img/s |
| FP-BNN [23] | Intel Stratix-V FPGA | 1160 μ s | 862 img/s |
| O3BNN [25] | Xilinx Zynq ZC706 FPGA | 774 μ s | 1292 img/s |
| SBNN [26] | NVIDIA Tesla V100 GPU | 979 μ s | 4400 img/s |
| BTC | NVIDIA RTX2080Ti GPU | 559 μ s | 4869 img/s |

TABLE 9: Comparing with CPU, GPU and FPGA using VGG-16 on ImageNet.

| Vgg-16/ImageNet | Platform | Raw Latency | Throughput |
|-----------------|------------------------|-------------|------------|
| BitFlow [41] | NVIDIA GTX1080 | 12.87 ms | 78 img/s |
| BitFlow [41] | Intel i7-7700 HQ | 16.10 ms | 62 img/s |
| BitFlow [41] | Intel Xeon-Phi 7210 | 11.82 ms | 85 img/s |
| O3BNN [25] | Xilinx Zynq ZC706 FPGA | 5.626 ms | 178 img/s |
| SBNN [26] | NVIDIA Tesla V100 GPU | 3.208 ms | 312 img/s |
| BTC | NVIDIA RTX2080Ti GPU | 3.570 ms | 1760 img/s |

that for *MLP*, a batch of 1024 is still insufficient for fully leveraging the bit-tensorcores, as will be discussed later. For *Alexnet*, the delay of the first layer remains too large (77.4%) while the other convolution layers are relatively smaller than alternative networks, which cannot fully utilize the BTCs. (II) Although showing better performance, the speedup led by the new FSB format is not as good as in BMM and BConv, the major reason is that both the batch size and the channels are relatively small ($batch \leq 1K$, $channels \leq 512$) which is not the region that the FSB format can demonstrate its best speedups (Section VII).

Table 8 and 9 compare the single image raw latency and throughput of our BTC-based new format design with existing BNN approaches for CPU, GPU, Xeon-Phi and FPGA using Alexnet and VGG-16 on ImageNet. As can be seen, our design achieves the best single-image raw latency and throughput on Alexnet, and more than 5 \times throughput enhancement on VGG-16 over the existing works as listed.

7.5 Sensitivity Study

To further investigate the performance delivery, we perform several sensitivity studies in this subsection.

Latency Breakdown: Figure 24 illustrates the percentage breakdown of the latency (measured by *clock()* on GPU)

TABLE 10: Layer-wise Synchronization Overhead.

| Sync | Mnist-MLP | Cifar10-vgg | Cifar10-ResNet14 | Alexnet | VGG | ResNet18 |
|------|-----------|-------------|------------------|---------|-------|----------|
| % | 8.26% | 14.10% | 13.20% | 1.36% | 1.72% | 5.67% |

for the inference of 8 images over the six models on the RTX-2080 GPU. Clearly, the first layer contributes the most delay for the three ImageNet models due significantly larger image size than the other two datasets. For AlexNet, the percentage can be as high as 77.4%. It is also over 35% for VGG-16 and ResNet-18. This is different from existing belief that the first layer is often not a big issue due to the least parameters and computation [2], [26]. The latency for other layers are roughly balanced.

Synchronization Overhead: As we enforce global synchronization through cooperative-groups per layer to ensure data consistency, such global synchronizations can introduce extra overhead and idle waiting of SMs. Table 10 shows the percentage of this synchronization overhead, which is measured by removing all the synchronization primitives. As can be seen, this overhead is the most for the medium network models, e.g., the two on Cifar10, which are 14.1% and 13.2%, respectively.

Shortcut Overhead: We then focus on the two ResNet models and measure the overhead incurred by handling the cross-layer residual. Figure 26 show the latency and throughput of the two ResNet models on RTX-2080 regarding four scenarios: (a) with residual; (b) save the residual without fetching them; (c) fetch the residual without saving them; and (d) without the residual at all. For ResNet-14 on Cifar10, if eliminating the residual-related operations, we can gain 9.7% speedup in latency and 14% in throughput. For ResNet-18 on ImageNet, we can gain 9.0% in latency and 8.3% in throughput.

Utilization: Finally we investigate the impact of batch size over the throughput. If the batch size is too small, the hardware such as the bit-tensorcores might be under-utilized. Figure 25 shows the inference throughput of the

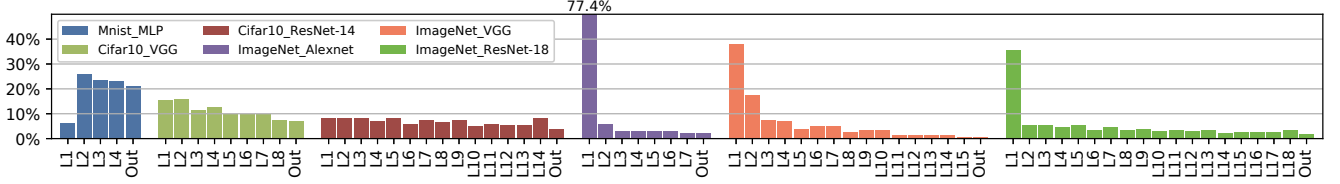


Fig. 24: Per-layer latency breakdown of our BTC new-format based BNN design on the 6 models.

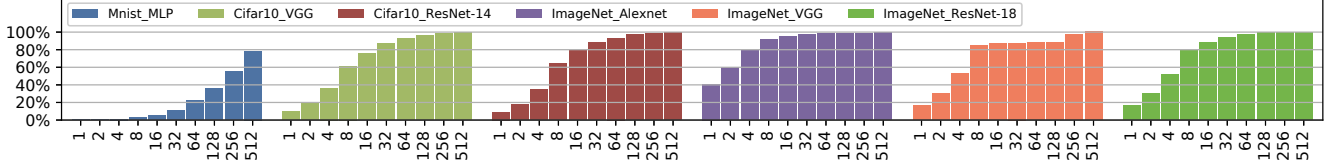


Fig. 25: Normalized throughput with respect to increased batch size for the BTC new-format BNN design on the 6 models.



Fig. 26: Cifar-ResNet14 Latency: 9.7% speedup, Throughput: 14%, ImageNet-ResNet18 Latency: 9.0% speedup, Throughput: 8.3%

six models with different batch sizes (normalized to the throughput with a batch of 1024 for MNIST and Cifar10, and 512 for ImageNet) on RTX2080. As can be seen, for ImageNet, a batch of 128 is sufficient to achieve the best throughput while for Cifar10, a batch of 512 is necessary. For MNIST, even with batch size arising from 16K to 32K, the throughput is still increasing. The maximum throughput is obtained at 32K, which is 7.62×10^6 fps.

8 CONCLUSION

In this paper we investigate and characterize the new bit computation capability of the tensorcores in NVIDIA Turing GPUs. We found that the stride of memory access can significantly impact the performance of memory access. Based on this observation, we propose a new bit data format for efficient design of Bit-Matrix-Multiplication and Bit-Convolution. We built the full implementation for the inference of binarized neural networks. Evaluations using six network models (MLP, VGG-like, AlexNet, VGG-16, ResNet-14/18) on three datasets (MNIST, Cifar10 and ImageNet) over two latest Turing GPUs (RTX2080 and RTX2080Ti) show that our design can bring on average $2.33 \times$ (up to $3.79 \times$) in latency and $1.81 \times$ (up to $2.84 \times$) in throughput compared with state-of-the-art BNN design for GPUs, leading to super realtime performance. As a future work, we are planning to exploit the bit-tensorcore for alternative utilization such as BLAS-based graph computation.

REFERENCES

- [1] Matthieu Courbariaux, Itay Hubara, Daniel Soudry, Ran El-Yaniv, and Yoshua Bengio. Binarized neural networks: Training deep neural networks with weights and activations constrained to +1 or -1. *arXiv preprint arXiv:1602.02830*, 2016.
- [2] Itay Hubara, Matthieu Courbariaux, Daniel Soudry, Ran El-Yaniv, and Yoshua Bengio. Binarized neural networks. In *Advances in Neural Information Processing Systems*, pages 4107–4115, 2016.
- [3] Mohammad Rastegari, Vicente Ordonez, Joseph Redmon, and Ali Farhadi. Xnor-net: Imagenet classification using binary convolutional neural networks. In *European Conference on Computer Vision*, pages 525–542. Springer, 2016.
- [4] Matthieu Courbariaux, Yoshua Bengio, and Jean-Pierre David. Binaryconnect: Training deep neural networks with binary weights during propagations. In *Advances in Neural Information Processing Systems*, pages 3123–3131, 2015.
- [5] Angus Galloway, Graham W Taylor, and Medhat Moussa. Attacking binarized neural networks. *arXiv:1711.00449*, 2017.
- [6] Elias B Khalil, Amrita Gupta, and Bistra Dilkina. Combinatorial attacks on binarized neural networks. *arXiv:1810.03538*, 2018.
- [7] Wei Tang, Gang Hua, and Liang Wang. How to train a compact binary neural network with high accuracy? In *AAAI*, 2017.
- [8] Sajad Darabi, Mouloud Belbahri, Matthieu Courbariaux, and Vahid Partovi Nia. BNN+: Improved binary network training. *arXiv preprint arXiv:1812.11800*, 2018.
- [9] Fayez Lahoud, Radhakrishna Achanta, Pablo Márquez-Neila, and Sabine Süsstrunk. Self-binarizing networks. *arXiv preprint arXiv:1902.00730*, 2019.
- [10] Zechun Liu, Baoyuan Wu, Wenhan Luo, Xin Yang, Wei Liu, and Kwang-Ting Cheng. Bi-real net: Enhancing the performance of 1-bit CNNs with improved representational capability and advanced training algorithm. In *Proceedings of the European Conference on Computer Vision (ECCV)*, pages 722–737, 2018.
- [11] Shilin Zhu, Xin Dong, and Hao Su. Binary ensemble neural network: More bits per network or more networks per bit? In *IEEE Conference on Computer Vision and Pattern Recognition*, 2019.
- [12] Joseph Bethge, Haojin Yang, Marvin Bornstein, and Christoph Meinel. BinaryDenseNet: Developing an Architecture for Binary Neural Networks. In *Proceedings of the IEEE International Conference on Computer Vision Workshops*, 2019.
- [13] Joseph Bethge, Christian Bartz, Haojin Yang, Ying Chen, and Christoph Meinel. MeliusNet: Can Binary Neural Networks Achieve MobileNet-level Accuracy? *arXiv:2001.05936*, 2020.
- [14] Pierre Baldi, Kyle Cranmer, Taylor Faucett, Peter Sadowski, and Daniel Whiteson. Parameterized machine learning for high-energy physics. *arXiv preprint arXiv:1601.07913*, 2016.
- [15] Buser Say and Scott Sanner. Planning in factored state and action spaces with learned binarized neural network transition models. In *IJCAI*, pages 4815–4821, 2018.
- [16] Svyatoslav Korneev, Nina Narodytska, Luca Pulina, Armando Tacchella, Nikolaj Bjorner, and Mooly Sagiv. Constrained image generation using binarized neural networks with decision procedures. In *International Conference on Theory and Applications of Satisfiability Testing*, pages 438–449. Springer, 2018.
- [17] Chao Ma, Yulan Guo, Yinjie Lei, and Wei An. Binary volumetric convolutional neural networks for 3-d object recognition. *IEEE Transactions on Instrumentation and Measurement*, (99):1–11, 2018.
- [18] Paul Covington, Jay Adams, and Emre Sargin. Deep neural networks for youtube recommendations. In *Proceedings of the 10th ACM conference on recommender systems*. ACM, 2016.
- [19] Xiangnan He, Lizi Liao, Hanwang Zhang, Liqiang Nie, Xia Hu, and Tat-Seng Chua. Neural collaborative filtering. In *Proceedings of the 26th International Conference on World Wide Web*. International World Wide Web Conferences Steering Committee, 2017.

- [20] Eriko Nurvitadhi, David Sheffield, Jaewoong Sim, Asit Mishra, Ganesh Venkatesh, and Debbie Marr. Accelerating binarized neural networks: comparison of FPGA, CPU, GPU, and ASIC. In *International Conference on Field-Programmable Technology*, 2016.
- [21] Yaman Umuroglu, Nicholas J Fraser, Giulio Gambardella, Michaela Blott, Philip Leong, Magnus Jahre, and Kees Visser. Finn: A framework for fast, scalable binarized neural network inference. In *Proceedings of International Symposium on Field-Programmable Gate Arrays*. ACM, 2017.
- [22] Ritchie Zhao, Weinan Song, Wentao Zhang, Tianwei Xing, Jeng-Hau Lin, Mani Srivastava, Rajesh Gupta, and Zhiru Zhang. Accelerating binarized convolutional neural networks with software-programmable FPGAs. In *Proceedings of International Symposium on Field-Programmable Gate Arrays*. ACM, 2017.
- [23] Shuang Liang, Shouyi Yin, Leibo Liu, Wayne Luk, and Shaojun Wei. FP-BNN: Binarized neural network on FPGA. *Neurocomputing*, 275:1072–1086, 2018.
- [24] Tong Geng, Tianqi Wang, Chunshu Wu, Chen Yang, Shuai-wen Leon Song, Ang Li, and Martin Herbordt. LP-BNN: Ultra-low-Latency BNN Inference with Layer Parallelism. In *Proceedings of the 30th IEEE International Conference on Application-specific Systems, Architectures, and Processors*. IEEE, 2019.
- [25] Tong Geng, Tianqi Wang, Chunshu Wu, Chen Yang, Wei Wu, Ang Li, and Martin C Herbordt. O3BNN: an out-of-order architecture for high-performance binarized neural network inference with fine-grained pruning. In *Proceedings of the ACM International Conference on Supercomputing*, pages 461–472. ACM, 2019.
- [26] Ang Li, Tong Geng, Tianqi Wang, Martin Herbordt, Shuai-wen Leon Song, and Kevin Barker. Bstc: a novel binarized-soft-tensor-core design for accelerating bit-based approximated neural nets. In *Proceedings of International Conference for High Performance Computing, Networking, Storage and Analysis*. ACM, 2019.
- [27] NVIDIA. NVIDIA Turing GPU Architecture, 2019.
- [28] Kumar Chellapilla, Sidd Puri, and Patrice Simard. High performance convolutional neural networks for document processing. In *Tenth International Workshop on Frontiers in Handwriting Recognition*. Suvisoft, 2006.
- [29] Sharan Chetlur, Cliff Woolley, Philippe Vandermersch, Jonathan Cohen, John Tran, Bryan Catanzaro, and Evan Shelhamer. cudnn: Efficient primitives for deep learning. *arXiv:1410.0759*, 2014.
- [30] Taylor Simons and Dah-Jye Lee. A review of binarized neural networks. *Electronics*, 8(6), 2019.
- [31] NVIDIA. CUDA Template Library for Dense Linear Algebra at All Levels and Scales (CUTLASS), 2018.
- [32] Wenbin Fang, Mian Lu, Xiangye Xiao, Bingsheng He, and Qiong Luo. Frequent itemset mining on graphics processors. In *Proceedings of the fifth international workshop on data management on new hardware*, pages 34–42. ACM, 2009.
- [33] Benjamin Block, Peter Virnau, and Tobias Preis. Multi-GPU accelerated multi-spin Monte Carlo simulations of the 2D Ising model. *Computer Physics Communications*, 181(9):1549–1556, 2010.
- [34] Martín Pedemonte, Enrique Alba, and Francisco Luna. Bitwise operations for GPU implementation of genetic algorithms. In *Proceedings of the 13th annual conference companion on Genetic and evolutionary computation*, pages 439–446. ACM, 2011.
- [35] Francesco Fusco, Michail Vlachos, Xenofontas Dimitropoulos, and Luca Deri. Indexing million of packets per second using GPUs. In *Conference on Internet measurement conference*. ACM, 2013.
- [36] Kefu Xu, Wenke Cui, Yue Hu, and Li Guo. Bit-parallel multiple approximate string matching based on GPU. *Procedia Computer Science*, 17:523–529, 2013.
- [37] Eli Ben-Sasson, Matan Hamilis, Mark Silberstein, and Eran Tromer. Fast multiplication in binary fields on GPUs via register cache. In *International Conference on Supercomputing*. ACM, 2016.
- [38] Jingkuan Song. Binary generative adversarial networks for image retrieval. *arXiv preprint arXiv:1708.04150*, 2017.
- [39] Saman Ashkiani, Martin Farach-Colton, and John D Owens. A dynamic hash table for the GPU. In *IEEE International Parallel and Distributed Processing Symposium (IPDPS)*. IEEE, 2018.
- [40] Bradley McDanel, Surat Teerapittayanon, and HT Kung. Embedded binarized neural networks. *arXiv:1709.02260*, 2017.
- [41] Yuwei Hu, Jidong Zhai, Dinghua Li, Yifan Gong, Yuhao Zhu, Wei Liu, Lei Su, and Jiangming Jin. BitFlow: Exploiting Vector Parallelism for Binary Neural Networks on CPU. In *International Parallel and Distributed Processing Symposium (IPDPS)*. IEEE, 2018.
- [42] Xiaofan Lin, Cong Zhao, and Wei Pan. Towards accurate binary convolutional neural network. In *Advances in Neural Information Processing Systems*, pages 345–353, 2017.
- [43] Norman P Jouppi, Cliff Young, Nishant Patil, David Patterson, Gaurav Agrawal, Raminder Bajwa, Sarah Bates, Suresh Bhatia, Nan Boden, Al Borchers, et al. In-datacenter performance analysis of a tensor processing unit. In *Proceedings of the 44th Annual International Symposium on Computer Architecture*. ACM, 2017.
- [44] NVIDIA. Volta Architecture White Paper, 2018.
- [45] Zhe Jia, Marco Maggioni, Benjamin Staiger, and Daniele P Scarpazza. Dissecting the NVIDIA Volta GPU architecture via microbenchmarking. *arXiv preprint arXiv:1804.06826*, 2018.
- [46] Zhe Jia, Marco Maggioni, Jeffrey Smith, and Daniele Paolo Scarpazza. Dissecting the NVIDIA Turing T4 GPU via Microbenchmarking. *arXiv preprint arXiv:1903.07486*, 2019.
- [47] Stefano Markidis, Steven Wei Der Chien, Erwin Laure, Ivy Bo Peng, and Jeffrey S Vetter. Nvidia tensor core programmability, performance & precision. In *International Parallel and Distributed Processing Symposium Workshops*. IEEE, 2018.
- [48] Md Aamir Raihan, Negar Goli, and Tor M Aamodt. Modeling Deep Learning Accelerator Enabled GPUs. In *International Symposium on Performance Analysis of Systems and Software*. IEEE, 2019.
- [49] Brian Hickmann and Dennis Bradford. Experimental Analysis of Matrix Multiplication Functional Units. In *26th Symposium on Computer Arithmetic (ARITH)*. IEEE, 2019.
- [50] Azzam Haidar, Stanimire Tomov, Jack Dongarra, and Nicholas J Higham. Harnessing GPU tensor cores for fast FP16 arithmetic to speed up mixed-precision iterative refinement solvers. In *Proceedings of the International Conference for High Performance Computing, Networking, Storage, and Analysis*, page 47. IEEE Press, 2018.
- [51] Anumeena Sorna, Xiaohe Cheng, Eduardo D’Azevedo, Kwai Won, and Stanimire Tomov. Optimizing the Fast Fourier Transform Using Mixed Precision on Tensor Core Hardware. In *2018 IEEE 25th International Conference on High Performance Computing Workshops (HiPCW)*, pages 3–7. IEEE, 2018.
- [52] Pierre Blanchard, Nicholas J Higham, Florent Lopez, Theo Mary, and Srikara Pranesh. Mixed Precision Block Fused Multiply-Add: Error Analysis and Application to GPU Tensor Cores. 2019.
- [53] Abdul Dakkak, Cheng Li, Jinjun Xiong, Isaac Gelado, and Wenmei Hwu. Accelerating reduction and scan using tensor core units. In *Proceedings of the ACM International Conference on Supercomputing*, pages 46–57. ACM, 2019.
- [54] NVIDIA. NVIDIA Tesla V100 GPU Architecture, 2017.
- [55] Guangming Tan, Linchuan Li, Sean Trichele, Everett Phillips, Yungang Bao, and Ninghui Sun. Fast implementation of DGEMM on Fermi GPU. In *Proceedings of International Conference for High Performance Computing, Networking, Storage and Analysis*, 2011.
- [56] NVIDIA. CUDA Programming Guide, 2018.
- [57] Sergey Ioffe and Christian Szegedy. Batch normalization: Accelerating deep network training by reducing internal covariate shift. *arXiv preprint arXiv:1502.03167*, 2015.
- [58] Kaiming He, Xiangyu Zhang, Shaoqing Ren, and Jian Sun. Deep residual learning for image recognition. In *Proceedings of the IEEE conference on computer vision and pattern recognition*, 2016.
- [59] Michael LeBeane, Khaled Hamidouche, Brad Benton, Mauricio Breternitz, Steven K Reinhardt, and Lizy K John. GPU triggered networking for intra-kernel communications. In *Proceedings of the International Conference for High Performance Computing, Networking, Storage and Analysis*, pages 1–12, 2017.
- [60] Yann LeCun, Corinna Cortes, and CJ Burges. MNIST handwritten digit database. *AT&T Labs [Online]*. Available: <http://yann.lecun.com/exdb/mnist>, 2, 2010.
- [61] Alex Krizhevsky, Vinod Nair, and Geoffrey Hinton. The CIFAR-10 dataset. online: <http://www.cs.toronto.edu/kriz/cifar.html>, 2014.
- [62] Jia Deng, Wei Dong, Richard Socher, Li-Jia Li, Kai Li, and Li Fei-Fei. Imagenet: A large-scale hierarchical image database. In *Conference on Computer Vision and Pattern Recognition*. IEEE, 2009.
- [63] Alex Krizhevsky, Ilya Sutskever, and Geoffrey E Hinton. ImageNet classification with deep convolutional neural networks. In *Advances in neural information processing systems*, 2012.
- [64] Karen Simonyan and Andrew Zisserman. Very deep convolutional networks for large-scale image recognition. *arXiv preprint arXiv:1409.1556*, 2014.
- [65] Mohammad Ghasemzadeh, Mohammad Samragh, and Farinaz Koushanfar. Rebnet: Residual binarized neural network. In *2018 IEEE 26th Annual International Symposium on Field-Programmable Custom Computing Machines (FCCM)*, pages 57–64. IEEE, 2018.